expected. Recall that we have reduced the 1–2% shrinkage tolerance commonly specified by laboratories to about a quarter by taking into account Ref. 10. However, the fabricated circuit has entirely exhausted the envisaged range. Yet, the insertion loss is still very good. Within the envisaged band, the reflection coefficient remains $< -10$ db, for 74.5 GHz and above at 77.5 GHz, very good values are achieved as well. Beyond these frequencies, $|S_{11}|$ reveals differences between simulation and measurements. Two reasons are most likely responsible: The second layer is to some extent more excited than in simulation, due to unfortunately slightly impaired vias (by the laser cutting process), which can be seen in the micrograph Figure 6. The second reason is the influence of the screwing of top and bottom RWG. At these frequencies, it produces some unavoidable nonalignment of the walls which causes some loss but also shows a slightly shifted $S_{11}$ result each time the RWG top and bottom parts are screwed together.

## 5. CONCLUSION

A new very practical millimeter-wave transition for joining an RWG with the first layer SIW of a two layer LTCC has been proposed. It addresses both the shrinkage tolerances typically seen with this material as well as the avoidance of a second layer excitation. The LTCC tan $\delta$ and $\varepsilon_r$ have been determined through a LINE and THRU measurement to distinguish the transition loss from the actual transmission line loss. These novel purely intrasubstrate experiments further confirm the strong dispersion of the LTCC. Simulations, with and without a varying gap, as well as the measurements on the fabricated back-to-back transition prove our concept. Fabricated LTCC circuits have been analyzed optically and even exceeded the total estimated shrinkage range. However, the transition shows good insertion loss $< 0.7$ dB and a good matching with RL $< 10$ dB in the envisaged band. These results allow recommending this transition for two layer LTCC SIW projects up to an approximate circuit length of 12 $\lambda_g$ in comparable environments.

## REFERENCES

1. H. Uchimura, T. Takenoshita, and M. Fujii, Development of a laminated waveguide, IEEE Trans Microwave Theory Tech 46 (1998), 2438–2443.
2. F. Xu and K. Wu, Guided-wave and leakage characteristics of substrate integrated waveguide, IEEE Trans Microwave Theory Tech 53 (2005), 66–73.
3. D. Deslandes and K. Wu, Accurate modeling, wave mechanisms, and design considerations of a substrate integrated waveguide, IEEE Trans Microwave Theory Tech 54 (2006), 2516–2526.
4. Q. Zhang and Y. Lu, E-band T shape transitions between substrate integrated waveguide and standard waveguide, Microwave Conference, 2008. APMC 2008. Asia-Pacific, 2008, pp. 1–4.
5. J.J. Lee, K.C. Eun, D.Y. Jung, et al. A novel GCPW to rectangular waveguide transition for 60 GHz applications, IEEE Microwave Wireless Compon Lett 19 (2009), 80–82.
6. B. Boukari, E. Moldovan, S. Affes, K. Wu, R.G. Bosisio, and S.O. Tatu, Robust microstrip-to-waveguide transitions for millimeter-wave radar sensor applications, IEEE Antennas Wireless Propag Lett 8 (2009), 759–762.
7. E. Moldovan, R.G. Bosisio, and K. Wu, W-band multiport substrate-integrated waveguide circuits, IEEE Trans Microwave Theory Tech 54 (2006), 625–632.
8. T. Baras and A. Jacob, Manufacturing reliability of LTCC millimeter-wave passive components, IEEE Trans Microwave Theory Tech 56 (2008), 2574–2581.
9. S. Adhikari, A. Stelzer, A. Springer, C. Wagner, C. Korden, and M. Stadler, Characterization of LTCC substrate up to 100 GHz, International Conference on Microwave and Millimeter Wave Technology, Vol. 4, 2008, pp. 1776–1779.
10. M. Girardi, Response predicting LTCC firing shrinkage: A response surface analysis study, J Microelectron Electron Packaging, 6 (2009)
11. L. Yan, W. Hong, G. Hua, J. Chen, K. Wu, and T.J. Cui, Simulation and experiment on SIW slot array antennas, IEEE Microwave Wireless Compon Lett 14 (2004), 446–448.
12. DuPont Green Tape—low temperature co-fired Ceramic system, online available at: http://www2.dupont.com/MCM/en_US/assets/downloads/prodinfo/GreenTape_Design_Layout_Guidelines.pdf
13. R. Kulke, M. Rittweger, P. Uhlig, and C. Günner, LTCC-Multilayer Ceramic for Wireless and Sensor Applications, IMST GmbH, online available at: http://www.ltcc.de/downloads/rd/pub/10-doc-plus-engl-2001.pdf
14. Federal Communications Commission FCC 11-79, 2011, online available at: http://hraunfoss.fcc.gov/edocs_public/attachmatch/FCC-11-79A1.pdf

# FDTD COMPUTATIONAL STUDY OF NANOPLASMONIC GUIDING STRUCTURES FOR NON-PARAXIAL SPATIAL SOLITONS

**Zachary Lubin, Jethro H. Greene, and Allen Taflove**
Department of Electrical Engineering and Computer Science, Northwestern University, Evanston, IL; Corresponding author: z-lubin@northwestern.edu

**ABSTRACT:** *Spatial solitons with beamwidths on the order of a wavelength are studied numerically in the context of their propagation paths being modified by planar nanoplasmonic structures. The prospect of such media in certain configurations used as soliton guiding devices is quantitatively assessed. A finite-difference time-domain model is used that incorporates a Kerr nonlinearity and linear dispersion, and solves for the vector components of the fields. A soliton effective beamsplitter, collimator, and dual-beam waveguide are demonstrated. Interesting aspects of the reflection and transmission properties of gold films is discussed, including first-time reporting of the Goos-Hänchen effect in the nonlinear regime for a transverse magnetic, ultra-narrow spatial soliton incident on a gold slab. The results provided herein are significant for nonlinear switching and routing applications toward future all-optical computing devices.* © 2012 Wiley Periodicals, Inc. Microwave Opt Technol Lett 54:2679–2684, 2012; View this article online at wileyonlinelibrary.com. DOI 10.1002/mop.27182

## 1. INTRODUCTION

Spatial solitons are optical beams that maintain their transverse profile with propagation, by balancing diffraction and self-focusing through intensity-induced modifications in the local refractive index. Initially discovered and studied in the 1960s, they have seen a resurgence in nonlinear optics research over the

past two decades due to their potential role in optical computing. There is a need to control the angular divergence of light as it propagates to maintain signal integrity, and also to efficiently manipulate beam routing in circuits approaching the nanometer scale. Solitons offer a natural focusing mechanism that can be exploited.

In recent years, studies have explored spatial soliton interactions with metals, leading to emergence of a so-called "soliton plasmonics" area. It is well established that incident electromagnetic waves on metallic media at optical wavelengths can induce electron oscillations, and at surfaces can excite surface waves known as surface plasmon polaritons (SPPs). Sharp resonances may be induced through this interaction process, depending on the incident polarization, material geometry, and wavevector, among other factors (for a nice overview of the field, see Ref. 1). These resonances can lead to enhanced, sub-wavelength evanescent fields in the SPPs, useful in many applications (e.g., see Refs. 2 and 3). These enhanced fields have important effects on spatial solitons. For example, it has been shown that using metal waveguides, power efficiency is attained in soliton generation [4]. Subwavelength discrete solitons can be formed in periodic metal-dielectric slabs from SPP tunneling [5]. Other studies have looked at SPP focusing by nonlinearities at interfaces and also resonant-based control of SPPs by adjacent solitons [6, 7].

An open research area is studying the characteristics of solitons as they impinge on metallic media such as nanoscale films, and their scattering, reflection, and transmission behavior—or particularly the problem of soliton guiding by such media. While it is intuitive that the beams should demonstrate behavior in accordance with the classical laws of reflection (i.e., should have large reflection and little transmission when incident on thick metal films), it is important to consider the fact that at optical wavelengths and nanoscale thicknesses, metals become increasingly transmissive and take on dielectric-like properties. Additionally, solitons of the non-paraxial or "ultra-narrow" type—having beamwidths on the scale of a dielectric wavelength—are far removed in nature from the conventional linear plane wave or Gaussian beam, and the vector electromagnetic field behavior involved with multiple scattering events can become extremely complex. To date (and the best of our knowledge), no studies have quantified the feasibility of guiding such narrow solitons using metallic media on scales that show complicated mixtures of both reflectivity and significant transmissivity. This is an important and worthwhile problem, since future all-optical nanocircuits will likely integrate metal structures in some capacity (perhaps intentionally for guiding, or inherent through fabrication).

In this article, we report on a study exploring the feasibility of guiding non-paraxial, transverse magnetic (TM) polarized spatial solitons using gold structures on the nanometer scale. The results were obtained through numerical experiments using a finite-difference time-domain (FDTD) computational electrodynamics model. The model provides vector field solutions directly from Maxwell's equations in time without simplifying assumptions, and rigorously includes dispersion and nonlinearity characteristics of the media. We consider four different experiments in particular—reflection of an obliquely incident soliton upon a thin gold film; a dual-reflection scheme using two gold films not necessarily of the same thickness; and a dual-soliton gold slab waveguide. These were chosen for their illustrative, fundamental reflection-transmission phenomena, and are not intended to represent a complete basis of possibilities for soliton routing media configurations but are believed to be directly applicable to numerous switching circuit applications.

## 2. FDTD GVADE MODEL

Our choice of FDTD for this study was based on several reasons. First, the complexity of the problem required a model that could accurately account for the vector components of the fields and not rely on any scalar approximations. The highly non-paraxial nature of the solitons in our experiments leads to a strong longitudinal electric field component and cannot be neglected [8]. Second, a model was needed that elegantly incorporated the dispersive nature of the host medium and the metals. Third, FDTD lends itself well to parallelization on a computing cluster to decrease simulation time. The spatial and time scales involved in the problem placed high demands from a computational perspective, so the ability to easily parallelize was a major consideration.

The model uses a recently developed algorithm known as the general vector auxiliary differential equation (GVADE) formulation, derived and verified in Ref. 9. It solves for multiple electric field components, and incorporates nonlinearities and both linear and nonlinear dispersions of the modeled media. GVADE was previously used to study the influence of scattering air holes on soliton propagation and also the interactions between a pair of copropagating non-paraxial solitons [10, 11].

A new variation on GVADE was introduced in this study through the incorporation of a linear dispersion for metallic media, based upon the Drude model. This models the linear relative permittivity as

$$\varepsilon(\omega) = \varepsilon_\infty - \frac{\omega_p^2}{\omega^2 - j\omega\gamma} \tag{1.1}$$

where $\omega_p$ is the plasma frequency, $\varepsilon_\infty$ is the high-frequency dielectric constant, $j = \sqrt{-1}$, and $\gamma$ is the inverse of the free-electron gas relaxation time. In regions where the metal resides, the electric field components are updated using the framework discussed in Ref. 12, and the remaining portions of the computational grid have their electric field components updated using the standard GVADE method. The parameters for gold used in Eq. (1.1) were $\omega_p = 1.3544 \times 10^{16}$ rad/s, $\gamma = 1.1536 \times 10^{14}$ rad/s, and $\varepsilon_\infty = 9.0685$ [13].

The surrounding medium of the gold, and propagation medium for the soliton, was silica glass. This has a third-order instantaneous (Kerr) nonlinearity with refractive index of the form $n = n_0 + n_2 I$, where $n_0$ is the linear refractive index ($\sim 1.45$ for silica) and the nonlinear index coefficient $n_2 = 2.48 \times 10^{-20}$ m$^2$/W [14]. The resonant strengths in the Sellmeier equation modeling the Lorentz linear dispersion were $\beta_1 = 0.6961663$, $\beta_2 = 0.4079426$, and $\beta_3 = 0.8974794$, and the resonant wavelengths were $\lambda_1 = 0.0684043$ $\mu$m, $\lambda_2 = 0.1162414$ $\mu$m, and $\lambda_3 = 9.896161$ $\mu$m [14]. The simulations in this study were two-dimensional, and considered two orthogonal electric field components $E_x$ and $E_y$ and one magnetic field component Hz (TM polarization). The computational grid size was made as large as possible, to avoid outgoing energy reflected from the boundaries from interfering with the solution domain of interest (as at this time no absorbing boundary condition is available for GVADE but is a future research endeavor). Details on the specific grid sizes used are given in the next section. A rectangular grid cell size of $\Delta = 10$ nm, resulting in 80 grid cells per free-space wavelength at 800 nm, was chosen based on convergence studies to balance geometrical feature resolution and accuracy.

The choice of time-step $\Delta t$ in an FDTD simulation is dictated by the Courant stability condition after the spatial resolution $\Delta$ is chosen [12]. This is given by $\Delta t \leq S\Delta/c$ for $S = 0.707$ for a 2D free-space grid where $c$ is the speed of light in vacuum, and
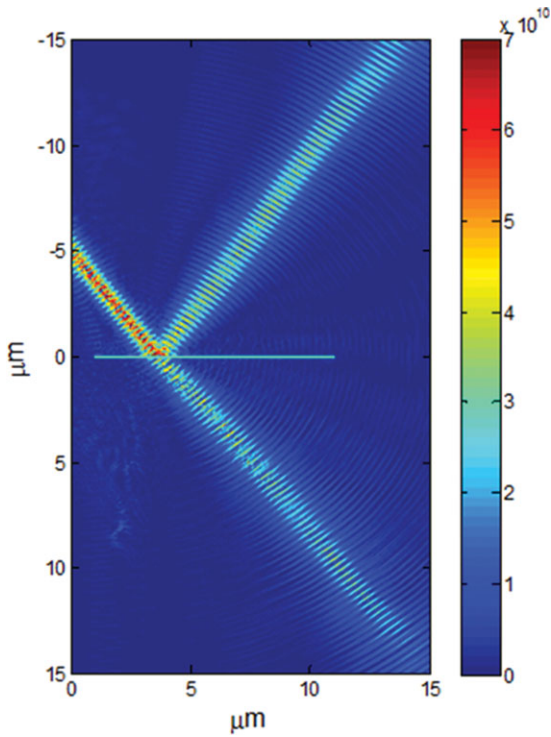
**Figure 1** E-field distribution. [Color figure can be viewed in the online issue, which is available at wileyonlinelibrary.com]

for $\Delta = 10$ nm, $\Delta t \leq 2.357 \times 10^{-17}$ s. The value of $\Delta t = 4.17 \times 10^{-18}$ s, over five times smaller than the classical definition, was empirically chosen for the simulations in this report based on convergence studies. We believe the reason for the discrepancy can be due to the significant differences in complexity between the classic linear FDTD algorithm and GVADE, a prime example being that at each time-step, a system of nonlinear equations must be iteratively solved at each grid point for the electric field.

The simulations were done in parallelized C++ utilizing an MPI library on an Intel Xeon 3.2 GHz 20-processor Linux cluster, and simulation times were typically under 24 h. Memory usage was typically on the order of 150 MB per process.

## 3. RESULTS AND DISCUSSION

The first experiment was the simplest of the configurations—a soliton impinging on a thin gold film of 20 nm thickness. The grid dimensions were 30 $\mu$m ($x$-dimension) by 60 $\mu$m ($y$-dimension). The soliton was sourced at the left edge of the FDTD grid by setting the Hz component equal to

$$H_z(i = 0, j, t) = A_0 u(t - j\tau) \sin[\omega_0(t - j\tau)] \text{sech}[\Delta(j - j_1)/w_0]$$
(1.2)

This represents a continuous wave beam with a transverse envelope following a hyperbolic secant profile. Here, $i$ is the index in the $x$-dimension (fixed at the left edge of the grid) and $j$ is the index in the $y$-dimension. $A_0$ is the magnetic field amplitude, $u(t)$ is the unit-step function, $\omega_0$ the frequency corresponding to a free-space wavelength of $\lambda_0 = 800$ nm, $j_1$ is the index in the $y$-dimension corresponding to the peak of the soliton transverse profile envelope, and $w_0$ is the characteristic beamwidth of the soliton. The parameter $\tau$ is a time constant that implements a linear delay taper across the Hz grid cells, enabling the sourcing of the soliton at an oblique angle $\theta$ with

respect to the propagation axis ($x$-dimension) where positive angles corresponded to downward directions as implemented in the model. Its form is

$$\tau = \frac{n_0 \Delta \sin \theta}{c}$$
(1.3)

The incident angle of the soliton was chosen to be $\theta = 57°$. This led to an angle of 33° with respect to the surface normal of the gold film. The characteristic beamwidth $w_0$ was chosen to be 261 nm. This gives an amplitude full-width at half-maximum (FWHM) of approximately 687 nm. The ratio of the FWHM to the dielectric wavelength (about 552 nm) is 1.25. The soliton beamwidth is narrow, approaching the size of a wavelength, and under these conditions starts to take on a non-paraxial quality requiring accounting of the vector nature of the fields in the simulation. Finally, the amplitude required for soliton generation was empirically determined through a series of numerical studies as $A_0 = 3 \times 10^8$ A/m.

Figure 1 shows the magnitude of the total electric field in the grid at a late time step into the simulation, long after the initial wavefront had reflected from the film surface. It is qualitatively evident that a significant amount of energy is permitted to transmit through the film, and is also of sufficient strength to enable the soliton to retain its form through the length of the run. The high transmissivity is essentially due to the thickness of the film being only on the order of one skin depth at 800 nm [15]. An interesting observation is that despite a fair amount of radiated diffractive energy in directions away from the soliton propagation direction, as seen in the figure, the soliton profile is retained. The distance the split soliton components propagate post-incidence is considerable, extending beyond 10 $\mu$m from the film in both the specular and refracted directions (on the order of 30 diffraction lengths, where $L_{\text{diff}} = \pi w_0^2/\lambda_d$.). Additional simulations showed the transmission ratio is easily reduced by simply increasing the film thickness toward 2 $\mu$m, rendering the film as a mirror (this will be apparent in later figures below).

We note the balanced nature of the energy between the transmission and reflection; an inspection of the |E| values in the grid confirmed that the field is essentially halved on both sides (on the order of 6 dB down from the field value near the peak of the beam), in general agreement with plane-wave Fresnel theory [16]. While the premise of a beam reflected by a thin film might seem rather simple, this configuration is observed to act as an effective non-paraxial soliton beamsplitter device, useful for a
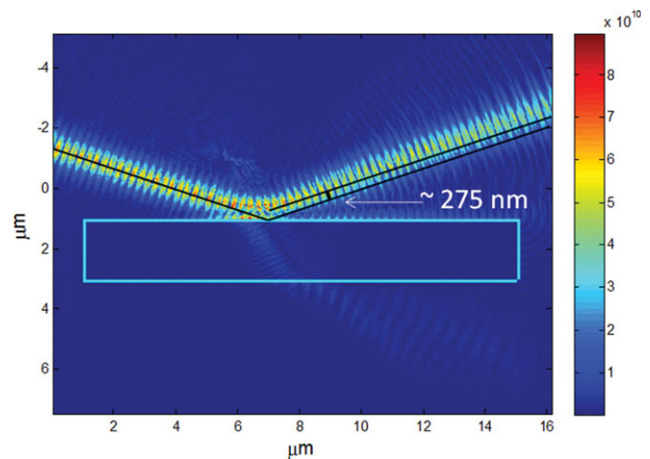


**Figure 2** Shift of reflection. [Color figure can be viewed in the online issue, which is available at wileyonlinelibrary.com]
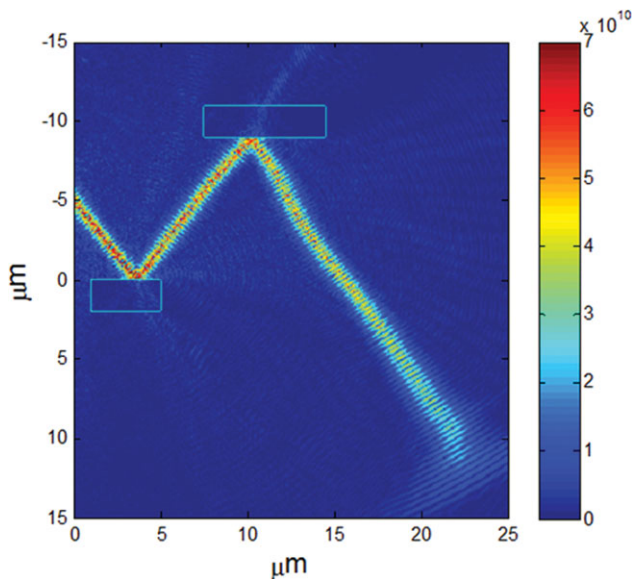
**Figure 3** Dual-mirror configuration. [Color figure can be viewed in the online issue, which is available at wileyonlinelibrary.com]

myriad of optical switching applications. Additionally, to the best of our knowledge, the proposal of a thin gold film as a soliton beamsplitter device has not been reported before in the literature. These results are also the first demonstration of GVADE FDTD capabilities of soliton-plasmonic material interaction modeling.

During various stages of this experiment, it was observed that for large angles with respect to the surface normal, and where the gold thickness was on the order of numerous skin depths, a lateral shift in the specular reflection in the plane of incidence occurred. This is shown in Figure 2 where the gold thickness was 2 $\mu$m and the incident angle relative to the surface normal was 70°. It is apparent that (as indicated by the overlaid black lines) the reflected soliton shows a lateral deviation from the expected location expected from Snell's law. This shift is estimated to be approximately 275 nm. This is a manifestation of the Goos-Hänchen effect, where the multiple plane wave components comprising the incident beam see different phase shifts at the surface. This effect was reported for a *linear* TM

polarized beam incident on gold in Ref. 17 and the shift of 300 nm reported therein is very similar to the shift we report here for the nonlinear case (with a narrow soliton).

The experimental observations on the thin film motivated other configurations to be investigated that have application to problems where there is a need for controlling the propagation direction of or combining non-paraxial spatial solitons. Consider Figure 3, where the gold film thickness has been increased to 2 $\mu$m. A second film of the same thickness was placed 9 $\mu$m above the first, and laterally shifted. This is a dual-mirror configuration where the incident soliton sees two reflection events at approximately 33° with respect to each film's surface normal. The grid simulation parameters and other beam characteristics were kept the same as the previous case.

Some interesting phenomena are observed; first, the soliton survives both reflections, retaining its transverse profile with propagation more than 25 diffraction lengths beyond the second film. Second, these results suggest dual thick gold films can enable lateral shifting (in this case to the right) of soliton propagation by more than 10 $\mu$m. An unexpected result was that the beam shows a divergence from a straight propagation direction shortly after the second reflection, yet later returns back to the initial course (Figure 3). A similar effect is slightly noticeable in the refracted energy beyond the upper film. The soliton trajectory can be strongly influenced by modulations in the local refractive index. Such modulations can be induced by material inhomogeneities or interactions with other close-proximity solitons, or by self-generated effects, that is, its own scattered fields may have sufficient intensity to influence the composite index in the region close to its propagation. Our hypothesis for the cause of the deviation from a straight propagation path is this latter effect. This in general will be a very complex interaction, as the superposition of the local soliton fields with those scattered by the films in the region between them will be constructive or deconstructive depending on their phase relationship and the resulting total intensity will dictate the effect on the soliton's course. Deeper investigation into this phenomenon is a planned topic for future research.

The two previous experiments were next combined to extend the applications of beamsplitting and lateral shift to a soliton collimator. Only a simple scaling of the first gold film was required, back to the 20 nm thickness, and a change in the location and separation of the upper film. Two variations were
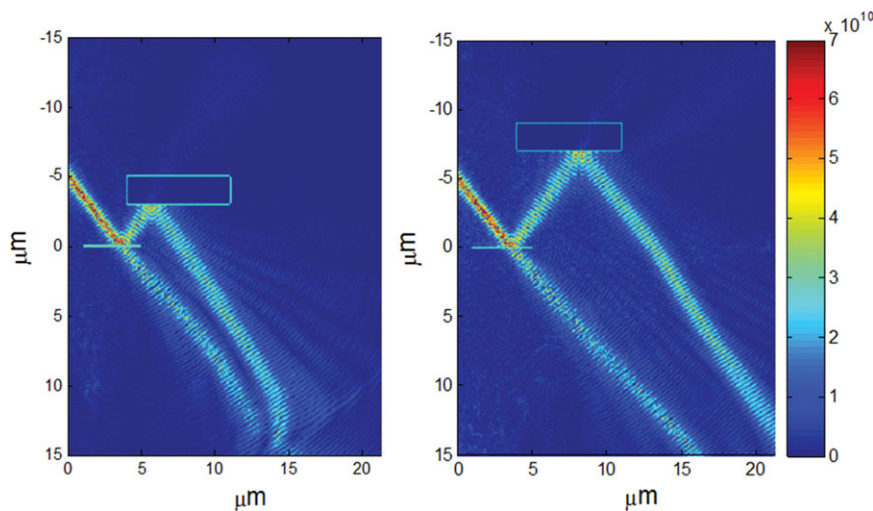


**Figure 4** Beam splitting experiments. [Color figure can be viewed in the online issue, which is available at wileyonlinelibrary.com]
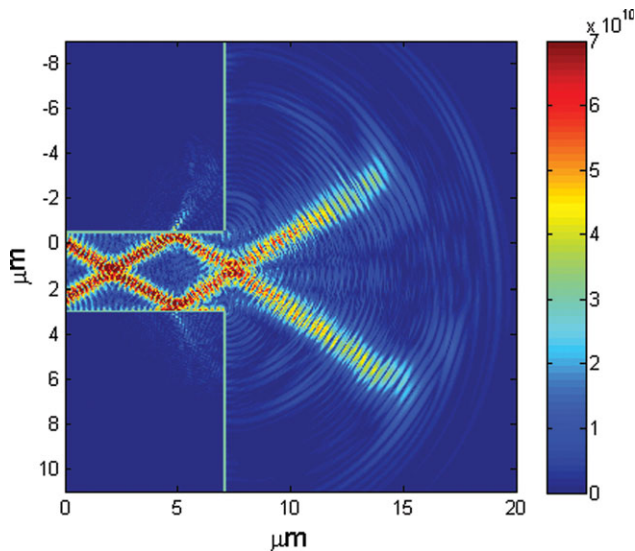
**Figure 5** Electric field at a late time step. [Color figure can be viewed in the online issue, which is available at wileyonlinelibrary.com]

considered—a separation of 3 $\mu$m and a separation of 7 $\mu$m, shown in Figure 4 left and right, respectively. The initial beam is split on striking the first film and the transmission continues as a soliton. The reflection, at roughly half the amplitude, is subsequently and nearly completely reflected by the upper, thicker slab back to a downward trajectory. Both beams ultimately follow an adjacent propagation trend, albeit not parallel. They tend to attract one-another and approach a meeting point depending on the film separation. These observations are similar to those presented in Ref. 11, where it was shown using GVADE FDTD that copropagating non-paraxial TM polarized solitons can attract each other depending on relative phase and separation distance. We hypothesize this phenomenon may be attributable to the combined effects of the dual-soliton interaction and the scattered fields from the films as suggested above.

The relevance of these results is that multiple gold slabs of varying thickness and separation can enable a configurable non-paraxial spatial soliton collimation device on the nanoscale. Orientation of the slabs allows control of the beam separation.

A final experiment focused on the case where the gold slabs were brought into close proximity and thickness dramatically increased to form a slab waveguide. The primary objective was to utilize the structure to simultaneously guide two solitons at oblique, complimentary angles with respect to the waveguide axis. Such a device meets application needs where multiple overlapping solitons require modifications in their propagation direction.

To mitigate the problem of having to source the solitons at a removed distance from the structure and collecting them into the guide aperture, while retaining sufficient guard distance from the surrounding grid boundaries, a new sourcing scheme was utilized. Instead of exciting the Hz field component, the magnetic current density $M_z$ was excited. While nonphysical, it is a valid mathematical approach to sourcing the field through Maxwell's equations. Furthermore, it resolved the issue of retro reflected energy from interfering with the source cells because $M_z$ is inherently transparent to the electric and magnetic fields.

The grid dimensions were 68 $\mu$m in the $x$-dimension and 50 $\mu$m in the $y$-dimension. In the center of the grid, two gold slabs were brought within close proximity to form a planar waveguide having a gap width of 3.5 $\mu$m and length of 14 $\mu$m. One soliton

was sourced at an angle of $\theta = 30°$ (downward) and the second was simultaneously sourced at $\theta = -30°$ (upward) in the center of the waveguide, with separation of 2.5 $\mu$m along the $y$-dimension. The pair were sourced using

$$M_z(i = 3400, j) = A_0 \frac{\mu_0}{\Delta t} u(t - j\tau_1) \sin[\omega_0(t - j\tau_1)]\mathrm{sech}[\Delta(j - j_1)/w_0]$$
$$+ A_0 \frac{\mu_0}{\Delta t} u(t - \tau_2(j - N_y + 1)) \sin[\omega_0(t - \tau_2(j - N_y + 1))]\mathrm{sech}[\Delta(j - j_2)/w_0]$$
(1.4)

The value of $i = 3400$ corresponds to the center of the grid along the $x$-dimension. $\tau_1$ and $\tau_2$ are given by (1.3) with $\theta = 30°$ and $-30°$, respectively. $A_0$ was empirically determined to be $5.0 \times 10^7$ A/m. $\mu_0$ is the free-space permeability, $N_y$ is the total number of grid cells in the $y$-dimension (5000), and $w_0$, $\omega_0$, and $\Delta t$ remained the same as the earlier experiments described above. The transverse peaks of the beams resided at $\Delta * j_1 = 25$ $\mu$m and $\Delta * j_2 = 27.5$ $\mu$m.

The magnitude of the total electric field at a late time step in the region of the waveguide is shown in Figure 5. Only one half of the grid is shown, as the other half is simply an image, and the left edge was relabeled to start at 0 $\mu$m (rather than 34 $\mu$m) to simplify reading the $x$-scale. Each beam sees a single reflection from the opposite side of the waveguide to reverse its direction, while intersecting paths with its dual. Each emerges from the guide in the opposite direction it originated at, retaining a focused envelope profile. Each beam could possibly be intercepted by a collection aperture, for example, for separation from the other beam. What results is an optical routing circuit where two overlapping solitons can be flipped in directions. This is the first reported proposal of a dual-soliton complimentary routing waveguide using gold.

## 4. CONCLUSIONS

The results presented here are believed to be the first quantitatively demonstrating that nanoplasmonic structures, specifically gold films and slabs, are feasible guiding devices for non-paraxial spatial solitons. It is also the first application of FDTD techniques to the problem where multiple electric field components and dispersions are fully accounted for. Finally, the study proposed gold structures as soliton beamsplitters, collimators, and dual-soliton waveguides, including reporting of an interesting observation of the Goos-Hänchen effect for the nonlinear case. Not only is this study relevant to efforts involved with time-domain numerical techniques for nonlinear electromagnetic fields, but also to switching and routing for nanoscale, all-optical computing applications. Future research includes deeper investigation into the role of scattered fields from the films on the soliton trajectory post reflection, and also the generation of SPPs using incident solitons.

### REFERENCES

1. S. Maier, Plasmonics: Fundamentals and applications, Springer, New York, NY, 2007.
2. C. Genet and T.W. Ebbesen, Light in tiny holes, Nature 445 (2007), 39–46.
3. E. Ozbay, Plasmonics: Merging photonics and electronics at nanoscale dimensions, Science 311 (2006), 189–193.

4. E. Feigenbaum and M. Orenstein, Plasmon-Soliton, Opt Lett 32 (2007), 674–676.

5. A. Marini, A.V. Gorbach, and D.V. Skryabin, Coupled-mode approach to surface plasmon polaritons in nonlinear periodic structures, Opt Lett 35 (2010), 3532–3534.

6. A.R. Davoyan, I.V. Shadrivov, and Y.S. Kivshar, Self-focusing and spatial plasmon-polariton solitons, Opt Express 17 (2009), 21732–21737.

7. K.Y. Bliokh, Y.P. Bliokh, and A. Ferrando, Resonant plasmon-soliton interaction, Phys Rev A 79 (2009), 418031–418033.

8. S. Chi and Q. Guo, Vector theory of self-focusing of an optical beam in Kerr media, Opt Lett 20 (1995), 1598–1600.

9. J.H. Greene and A. Taflove, General vector auxiliary differential equation finite-difference time-domain method for nonlinear optics, Opt Express 14 (2006), 8305–8310.

10. J.H. Greene and A. Taflove, Scattering of spatial optical solitons by subwavelength air holes, IEEE Microwave Wireless Comp Lett 17 (2007), 760–762.

11. Z. Lubin, J.H. Greene, and A. Taflove, FDTD computational study of ultra-narrow TM non-paraxial spatial soliton interactions, IEEE Microwave Wireless Comp Lett 21 (2011), 228–230.

12. A. Taflove and S.C. Hagness, Computational electrodynamics: The finite-difference time-domain method, 3rd ed., Artech House, 2005.

13. A. Vial, A. Grimault, D. Macias, D. Barchiesi, and M. Chapelle, Improved analytical fit of gold dispersion: Application to the modeling of extinction spectra with a finite-difference time-domain method, Phys Rev B 71 (2005), 854161–854167.

14. S. Nakamura, N. Takasawa, and Y. Koyamada, Comparison between finite-difference time-domain calculation with all parameters of Sellmeier's fitting equation and experimental results for slightly chirped 12 fs laser pulse propagation in a silica fiber, IEEE J Lightwave Technol 23 (2005), 855–863.

15. S. Kawata and V.M. Shalaev, Tip enhancement, Elsevier, 2007.

16. O.S. Heavens, Optical properties of thin solid films, Dover, 1991.

17. M. Merano, A. Aiello, G.W. t'Hooft, M.P. van Exter, E.R. Eliel, and J.P. Woerdman, Observation of Goos Hänchen shifts in metallic reflection, Opt Express 15 (2007), 15928–15934.

# REDUCED MICROSTRIP SLOT MULTIBAND ANTENNA WITH A U-SHAPED RESONATOR FOR WLAN APPLICATIONS

**R. Flores-Leal,[1] H. Jardon-Aguilar,[1] A. Tirado-Mendez,[2] and R. Acevo-Herrera[3]**
[1] Telecommunications Section, CINVESTAV-IPN, Mexico, D.F., Mexico 07360; Corresponding author: rfleal@cinvestav.mx
[2] Postgrade Studies and Research Section ESIME-IPN, Mexico, D.F., Mexico 07378
[3] Remote Sensing Lab, Department of Signal Theory and Communications, UPC Campus Nord D3, E-08034 Barcelona, Spain

**ABSTRACT:** *The development of two reduced microstrip slot antennas with a U-shaped resonant configuration is presented. The additional resonator is located inside the slot and is designed to perform dual band operation, covering the 2.4 GHz and 5.8 GHz WLAN frequency bands. The main goal of the antenna design is to get the optimum size reduction without significant degradation of electrical characteristics compared to a similar antenna reported in literature. The antenna implementation was done using low cost substrates. A size reduction of 84% was got by using a dielectric constant substrate of 10. Simulation and experimental results are presented for both antennas, showing close convergence. Their radiation patterns have quasi-omnidirectional behavior useful for WLAN applications. Both antennas have small size suitable for mobile applications.* © 2012 Wiley Periodicals, Inc. Microwave Opt Technol Lett 54:2684–2689, 2012; View this article online at wileyonlinelibrary.com. DOI 10.1002/mop.27187

## 1. INTRODUCTION

Nowadays, mobile communications are everywhere, they demand smaller antennas with better performance, to achieve all the features needed in communication systems, including low cost, small volume, and portability. Furthermore, in many occasions, they demand multiband characteristics to cover efficiently the required bands.

The combination of resonant structures with microstrip line slot antennas and tuning stubs, to efficiently match some desired bands, has been studied in several articles [1–8]. In Ref. 9, an interesting rectangular slot antenna with a U-shaped strip for WLAN communication is presented, improving broadband matching over the standard specifications. Nevertheless, the size of this prototype is not well suited for personal devices, as the total antenna area is $75 \times 75$ mm$^2$.

Here, it is proven that using low dielectric constant substrates, microstrip slot antennas with a U resonator can be significantly reduced, operating in 2.4 GHz and 5.8 GHz frequency bands for a $S_{11} \leq -10$ dB.

After a tuning procedure using CST Microwave Studio [10], it is found that there is a set of parameters involved in the performance of the antenna in Ref. 9, which can be modified to reduce the size of the device to operate in the required bands (2.4 and 5.8 GHz) without degrading the main parameters of the antenna, especially the gain, matching and radiation pattern.

Once several computer simulation processes were made, an optimum set of parameters was found for an antenna built over a substrate with a dielectric constant of 2.2. As a result, a 71.5% smaller antenna area was obtained. Using a substrate with higher dielectric constant for further size reduction, a second one was developed with an $\varepsilon_r = 10$. Following a similar tuning procedure used with the first antenna, a size reduction of 84% was got. These reduction factors of the antenna area are in contrast with the one reported in Ref. 9. Nevertheless, the small size, the performance is comparable to other reduced antennas available in the literature [11–19].

## 2. ANTENNA DESIGN

Figure 1 illustrates the configuration of the developed antennas. A 50-$\Omega$ microstrip line is used as a feeding line. On the ground plane, a rectangular slot is etched and also a U-shaped resonator is introduced to achieve the dual band operation. It performs as an extra resonator and it is centered inside the rectangular slot as it is depicted in Figure 1. Figure 2 shows the fabricated hardware.

The size of the rectangular slot given by $L_s$ and $W_s$ determines the lower band. The U-shaped structure is used as a resonant element to produce the second frequency band that can be controlled, mainly, by the length $L_1$. The longitude of the microstrip feed line $L_f$ determines the coupling of the rectangular slot with the resonator.

To reduce the antenna dimensions, a tuning process has to be carried out to determine the best size of the slot, the ground plane, and the length of the feeding line.

## 3. DEVELOPMENT AND RESULTS

After several tuning processes, the best parameters for the first antenna were obtained. This one was fabricated on substrate with $\varepsilon_r = 2.2$ (Taconic TLY-5), its thickness, $h$, is 1.27 mm.